AD_____

Award Number: DAMD17-98-1-8068

TITLE: A Novel Ultrasonic Imaging Method for Remote Palpation of Breast Tissues

PRINCIPAL INVESTIGATOR: Gregg E. Trahey, Ph.D.

CONTRACTING ORGANIZATION: Duke University,
Durham, North Carolina 27708

REPORT DATE: September 2000

TYPE OF REPORT: Annual

PREPARED FOR: U.S. Army Medical Research and Materiel Command
Fort Detrick, Maryland 21702-5012

REPORT DOCUMENTATION PAGE

Form Approved
OMB No. 074-0188

1. AGENCY USE ONLY (Leave blank)	2. REPORT DATE	3. REPORT TYPE AND DATES COVERED
	September 2000	Annual (1 Sep 99 - 31 Aug 00)

4. TITLE AND SUBTITLE
A Novel Ultrasonic Imaging Method for Remote Palpation of Breast Tissues

5. FUNDING NUMBERS
DAMD17-98-1-8068

6. AUTHOR(S)
Gregg E. Trahey, Ph.D.

7. PERFORMING ORGANIZATION NAME(S) AND ADDRESS(ES)
Duke University
Durham, North Carolina 27708

E-MAIL:
gregg.trahey@duke.edu

8. PERFORMING ORGANIZATION REPORT NUMBER

9. SPONSORING / MONITORING AGENCY NAME(S) AND ADDRESS(ES)
U.S. Army Medical Research and Materiel Command
Fort Detrick, Maryland 21702-5012

10. SPONSORING / MONITORING AGENCY REPORT NUMBER

11. SUPPLEMENTARY NOTES
This report contains colored photos

12a. DISTRIBUTION / AVAILABILITY STATEMENT
Approved for public release; distribution unlimited

12b. DISTRIBUTION CODE

13. ABSTRACT ***(Maximum 200 Words)***

A method of Remote Palpation, which may allow the detection of small, stiff lesions lying deep within the breast, is under investigation. In this method, acoustic radiation force is applied to localized (approximately 2 mm^3) regions of tissue, and the resulting tissue displacements are mapped using ultrasonic correlation based methods. Tissue displacement is inversely proportional to tissue stiffness, thus a stiffer region of tissue exhibits smaller displacements than a more compliant region. The resulting displacement maps are directly correlated with tissue stiffness.

We have developed finite element models of tissue mechanical and thermal response to acoustic radiation force. We have developed phantom fabrication facilities, and mechanical property measurement facilities, with which calibrated tissue phantoms have been developed. We have implemented acoustic Remote Palpation using multiple forcing locations in such phantoms, which resulted in high resolution, high contrast images of local variations in material stiffness. Finally, we have obtained preliminary clinical Remote Palpation data.

14. SUBJECT TERMS 1) Breast Cancer; 2) Acoustic Radiation Force; 3) Ultrasound Phantoms; 4) Tissue Young's Modulus; 5) Elastography	15. NUMBER OF PAGES 57
	16. PRICE CODE

17. SECURITY CLASSIFICATION OF REPORT	18. SECURITY CLASSIFICATION OF THIS PAGE	19. SECURITY CLASSIFICATION OF ABSTRACT	20. LIMITATION OF ABSTRACT
Unclassified	Unclassified	Unclassified	Unlimited

Contents

4 Introduction

The early detection of breast cancer reduces patient mortality. The most common method of breast cancer detection is palpation. However, lesions that lie deep within the breast are difficult to palpate when they are small. Thus, a method of Remote Palpation, which may allow the detection of small lesions lying deep within the breast, is currently under investigation. In this method, acoustic radiation force is used to apply localized (on the order of 2 mm^3) forces within tissue, and the resulting tissue displacements are mapped using ultrasonic correlation based methods. An area that is stiffer than the surrounding medium distributes the force, resulting in larger regions of displacement, and smaller maximum displacements. The resulting displacement maps are directly correlated with local tissue stiffness. In the second year of support, we have expanded our finite element models of tissue mechanical response to radiation force; we have developed finite element models of tissue thermal response to acoustic radiation force; we have performed experiments that validate the mechanical finite element model; we have constructed calibrated tissue phantoms and methods for measuring their mechanical properties, we have implemented acoustic Remote Palpation using multiple pushing locations in phantoms, and we have obtained initial clinical data.

5 Body

We have developed a finite element model of Remote Palpation, which has been validated experimentally [2, 1, 3]. The results of our phantom experiments and simulations are summarized in Appendices 10.1 and 10.2. This represents completion of Task 1 of the statement of work.

We have fabricated multiple phantoms with varying Young's modulii, with embedded lesions of varying sizes, and we have measured the Young's moduli of these phantoms. We have developed pulse sequences on the Siemens Elegra scanner to implement Remote Palpation in a single pushing location, and we have utilized an automated translation stage to translate the transducer in order to use this pulse sequence to interrogate an extended Field-of-View (FOV). Using the experimental setup, we have implemented Remote Palpation in phantoms using multiple pushing locations, and created the first Remote Palpation image of an embedded lesion. This image exhibited increased contrast over the corresponding ultrasonic B-mode image [3] (Appendix 10.2). These experiments and results represent completion of Task 2 of the statement of work.

We have developed a finite element model of the thermal response of tissue to acoustic radiation force, and have performed initial simulations (Figure 1). These simulations indicate that the spatial extent of the heating is limited to the focal region of the acoustic beam, and that the maximum increases in temperature will be less than 1°C during method implementation 1. This represents partial completion of Task 3 of the statement of work. Further simulations are required to investigate the different pulsing sequences that will be developed for further clinical implementation.

We have initiated clinical trials of the Remote Palpation method. Three patients have been imaged to date. Detectable tissue displacements were generated in one of the patients ($\sim$ 6

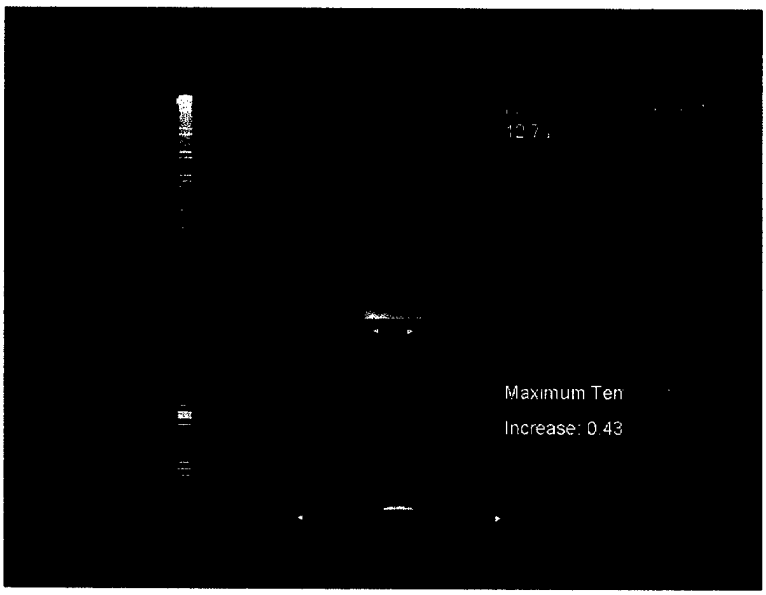

Figure 1: Top: Simulated displacement profile, and Bottom: simulated temperature increases resulting from a typical remote palpation beam sequence (*in vitro* I_{spta} = 250 W/cm^2, Tissue Young's modulus = 3.0 kPa). Note the different spatial scales on the two images. The yellow contour in the temperature plot is approximately the size of the pushing region of the acoustic beam. The shape of the white region in the displacement plot is similar to that of the focal region, although it is more broad. This is due to the shear stresses present in the medium (*i.e.* the tissue 'drags' the regions of tissue that surround the region where the force is applied). The relatively small temperature increases (light blue through red regions, maximum increase 0.43°C) are limited to the focal region of the acoustic beam. The transducer is on the left side of these images.

microns, Figure 2). This comprises partial completion of Task 4 of the statement of work. We have determined from these trials that further modifications are required in the beam sequences and the system power supplies in order to generate the required acoustic radiation forces in breast tissue. Even so, we are encouraged by the results to date, and are working to overcome the challenges that have been identified.

6 Key Research Accomplishments

- Enhanced finite element model of radiation force induced tissue motion.
- Developed finite element model of the thermal response of tissue to radiation force.
- Developed calibrated tissue phantoms.
- Developed measurement methods and measured the mechanical properties of the tissue phantoms.
- Developed experimental pulse sequences to implement Remote Palpation using multiple pushing locations.
- Implemented Remote Palpation with multiple pushing locations in phantom.

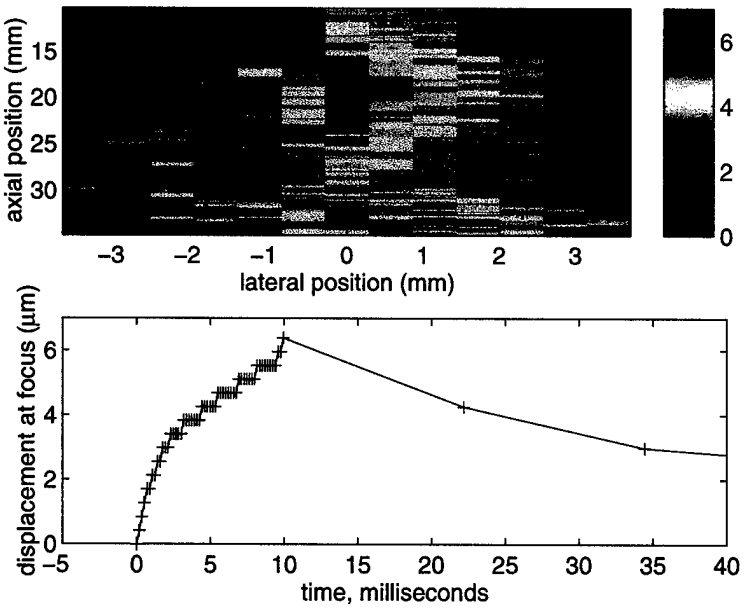

Figure 2: TOP: *In vivo* displacement image after 10 milliseconds of pushing in a single pushing location in: a) breast (33 year old female). The tracking beams were spaced 0.6 mm apart, and were sequenced to track laterally in the center, then out to the right, then back from center to left. The tissue begins to relax during the tracking sequences, which is the reason for the larger displacements on the right side than the left. BOTTOM: Corresponding displacement through time at the focal point of the transducer. **This image constitutes the first *in vivo* RP image.** Note that this displacement was achieved at a pushing pulse duty cycle of 3.4%. Significantly higher displacements are expected for an equivalent power, 100% duty cycle pushing pulse. The estimated intensity of the pushing beams was 240 W/cm^2, and an F/1 focal configuration was used. These experiments were performed using a non-attenuating standoff pad (10 mm).

- Generated the first Remote Palpation images using this data.
- Initiated clinical trials of the method.

7 Reportable Outcomes

- Paper published in *Ultrasonic Imaging*, entitled: "A finite element model of Remote Palpation of breast lesions using radiation force: factors affecting tissue displacement."
- Paper submission to *Journal of the Acoustical Society of America*, entitled: "On the feasibility of remote palpation using acoustic radiation force".
- Poster at the DOD BCRP Era of Hope meeting, in Atlanta, GA (June 8-11, 2000) entitled: "Acoustic Remote Palpation: Initial Simulation and Experimental Results"
- Presentation at the Twenty-fifth international symposium on ultrasonic imaging and tissue characterization in Arlington, Va (May 24, 2000) entitled: "An experimental

investigation of the Required Acoustic Power for In Vivo Implementation of Radiation Force Based Imaging."

- Presentation at the 2000 Annual Convention of the American Institute of Ultrasound in Medicine in San Francisco, CA (April 5, 2000) entitled: "Acoustic radiation force induced motion to characterize variations in tissue stiffness: initial experimental results."

- Presentation at the 1999 IEEE International Ultrasonics symposium at Lake Tahoe, NV (October 19, 1999) entitled: "Finite element analysis of radiation force induced tissue motion with experimental validation."

- Patent application filed, entitled: "Method and Apparatus for the identification and characterization of regions of altered stiffness".

- Whitaker grant application filed, and awarded, with funding to begin in September 2001, entitled: "A Radiation Force Based Ultrasonic Imaging System for the Early Detection of Breast Cancer".

8 Conclusions

The clinical implications of the results obtained during the second year of support are promising. The simulations and experimental results are consistent, and provide the framework for the design of a Remote Palpation imaging system. The first Remote Palpation image was created using multiple pushing locations to interrogate an extended field-of-view (FOV) in a calibrated phantom with and embedded lesion. This image showed increased contrast over the matched ultrasonic B-mode image. The initial thermal model results indicate that increases in tissue temperature during method implementation will be less than 1°C, which is within the FDA guidelines. The initial clinical data indicates that increases in acoustic power output and modifications in the temporal power distribution will be required for clinical implementation of the method. Key issues requiring further investigation include: thermal and power issues, development of pulse sequences with varying temporal power distributions, and investigation of methods of information display.

9 Bibliography

References

[1] K.R. Nightingale, R.W. Nightingale, M.L. Palmeri, and G.E. Trahey. Finite element analysis of radiation force induced tissue motion with experimental validation. In *Proceedings of the 1999 IEEE Ultrasonics Symposium*, pages 1319–1323, 1999.

[2] K.R. Nightingale, R.W. Nightingale, M.L. Palmeri, and G.E. Trahey. A finite element model of remote palpation of breast lesions using radiation force: Factors affecting tissue displacement. *Ultrasonic Imaging*, 22(1):35–54, January 2000.

[3] K.R. Nightingale, M.L. Palmeri, R.W. Nightingale, and G.E. Trahey. On the feasibility of remote palpation using acoustic radiation force. *J. Acoust. Soc. Am.*, in submission.

10 Appendices

10.1 Proceedings from IEEE UFFC meeting

FINITE ELEMENT ANALYSIS OF RADIATION FORCE INDUCED TISSUE MOTION WITH EXPERIMENTAL VALIDATION

Kathryn Nightingale, Roger Nightingale, Mark Palmeri, and Gregg Trahey

Duke University Department of Biomedical Engineering
Durham, NC 27708
kathy.nightingale@duke.edu

ABSTRACT

An ultrasonic radiation force-based method for remote palpation of tissue is investigated. The use of radiation force to image tissue stiffness has been proposed by several researchers. In this paper, the potential for using a diagnostic ultrasound system to both apply radiation force and track the resulting tissue displacements is investigated using Finite Element Methods (FEM), and the results are compared with experimental results. Remote palpation is accomplished by interspersing high intensity pushing beams with low intensity tracking beams. This generates localized radiation forces which can be applied throughout the tissue, with the resulting displacement patterns determined using correlation techniques. An area that is stiffer than the surrounding medium distributes the force, resulting in larger regions of displacement, and smaller maximum displacements. The resulting displacement maps provide information as to the location and size of regions of increased stiffness.

We have developed an FEM model that predicts displacements resulting from acoustic radiation force fields generated by diagnostic transducers in various complex media. We perform a parametric analysis of varying tissue and acoustic beam characteristics on radiation force induced tissue displacements. Displacements are on the order of microns, with considerable differences in displacement patterns in the presence and absence of a lesion (or stiff inclusion). Initial experimental results are presented that support the findings in the model.

1. INTRODUCTION

One of the most successful methods of early breast cancer detection is palpation. This is because the Young's modulus (*i.e.* stiffness) of malignant tumors is often an order of magnitude greater than that of normal breast tissue [15, 5]. Therefore, cancerous lesions feel 'harder' or 'stony' as compared to normal breast tissue. Several imaging modalities are under investigation that provide information about the stiffness of tissue. These include elastography, in which local variations in tissue strain are determined by measuring local displacements that occur during global tissue compression [15, 12, 11], and sonoelasticity, in which low frequency shear wave propagation is imaged using Doppler methods, from which the elastic modulus (Young's modulus) of tissue can be estimated [22, 6, 13, 4, 7].

The use of acoustic radiation force to image tissue stiffness is a fairly new concept that appears to hold some promise [14, 20, 18, 9, 2]. All of the proposed methods involve using radiation force to displace tissue in a remote location, and monitoring the tissue response. However, they differ in both system design and tissue response characterization.

Acoustic radiation force is a phenomenon associated with the propagation of acoustic waves through a dissipative medium. It is caused by the energy density gradient that occurs in the medium, arising either from absorption or reflection of the wave [19]. This gradient results in the application of a force in the direction of wave propagation. In an absorbing medium, and under plane wave assumptions, this force can be represented by the following equation [19, 10, 1, 17]:

$$F = \frac{W_{absorbed}}{c} = \frac{2\alpha I}{c}, \qquad (1)$$

where F is acoustic radiation force [kg/(s^{2}cm^2)], or [dynes/(1000 cm^3)]. $W_{absorbed}$ [Watts/(100 cm^3)] is the power absorbed by the medium at a given point in space, c [m/s] is the speed of sound in the medium, α [m^{-1}] is the absorption coefficient of the medium, and I [Watts/cm^2] is the temporal average intensity at a given point in space. Equation 1 provides a simple relationship between the temporal average intensity of an acoustic beam, and the resulting radiation force (which is in the form of a body force, or force per unit volume).

The method under investigation herein is called Remote Palpation. In this method, a single transducer on a diagnostic ultrasound system is used to apply localized (on the order of 2 mm^3) radiation forces within tissue, and to track the resulting tissue displacements which are determined using ultrasonic correlation based methods. An area that is stiffer than the surrounding medium distributes the force, resulting in larger regions of displacement, and smaller maximum displacements. This study was designed to determine the feasibility of Remote Palpation. A Finite Element Model (FEM) is presented with which a parametric analysis of varying tissue and acoustic beam parameters is performed. Initial experiments designed per the FEM findings are also presented, which provide good agreement with the simulations.

2. SIMULATION METHODS

Model implementation is performed using a two step approach: first the spatially distributed intensity field from a given trans-

This work was supported by DOD/BCRP grant BC972755. We thank Dr. Tim Hall of the University of Kansas for his support in phantom design; Dr. Bruce McDermott and Ms. Cindy Kerby of Siemens Medical Systems, Ultrasound Group for their system support; Altair Computing, Inc. for their meshing and post-processing support, and Intel Corporation for their technical and in-kind support.

0-7803-5722-1/99/$10.00

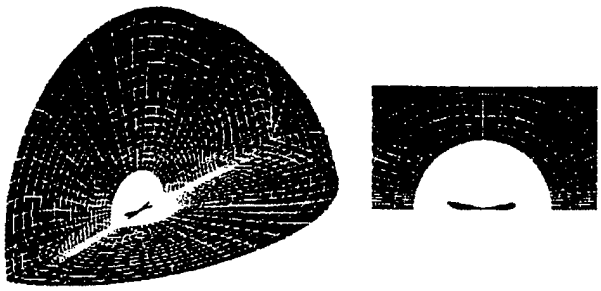

Figure 1: Left: Finite element mesh. The transducer is on the left (back) side of the page, with its axial dimension along the central axis of the mesh. The diameter of the outer hemisphere is 5 cm, and is intended to represent an effectively infinite boundary condition. Right: Magnified version of the central plane of the mesh, showing the increased element density in the focal region, the radiation force field contours for the F/1 transducer configuration, and the outline of a spherical 1.0 cm diameter lesion.

ducer and set of transmit parameters is determined and the associated radiation force field is computed using Equation 1. Second, finite element methods are used to solve for the resulting tissue displacement patterns.

FIELD_II (http://www.it.dtu.dk/~jaj/field/) [3], an acoustic field simulation program, was used to model the temporal average intensity patterns corresponding to various diagnostic transducer configurations. The transducer specifications were selected to model the Siemens 75L40 linear transducer array (center frequency 7.2 MHz, element height 5 mm, aperture width dependent upon the number of active elements; Siemens Medical Systems, Ultrasound Group, Issaquah, WA). The simulated voltage used to excite each element was fixed; thus, when more elements were excited, more energy was transmitted. The transducer was focused laterally at the location of its elevation focal point (which is determined by its lens).

The intensity fields for each transducer configuration (or f-number, which is the parameter we use as an indication of the number of elements included in the transmit aperture) were computed in the axial/lateral plane of the transducer and discretized into three contours of constant intensity. Once the contours and the desired boundaries were in place, they were imported into a finite element mesh generation program (Hypermesh, Altair Computing Inc., Troy, MI). The mesh was generated within this plane, and then rotated 90 degrees around its central axis, in order to achieve a three dimensional model (Fig. 1). The model was constrained on the surface of the distal quarter of the hemisphere (opposite the transducer location), thus modeling a breast resting on a concave platform. Because the boundary conditions did not allow motion normal to the planar surfaces in Figure 1, symmetry assumptions hold, and solution of this mesh simulates motion in one quarter of the axi-symmetric three dimensional spherical model. For the parametric analysis, the radiation force value applied within each intensity contour was computed using Eq. (1). Peak *in situ* intensities of 90 W/cm^2 and 15.3 W/cm^2 were used for the F/1 and F/3 transducer configurations, respectively. The speed of sound was 1530 m/s, and the absorption coefficient was .415 cm^{-1}, or 0.5 dB/cm/MHz. The resulting maximum body forces were 4882 and 830 dynes/cm^3, for the F/1 and F/3 transducer configurations, respectively. The density was 1000 kg/m^3,

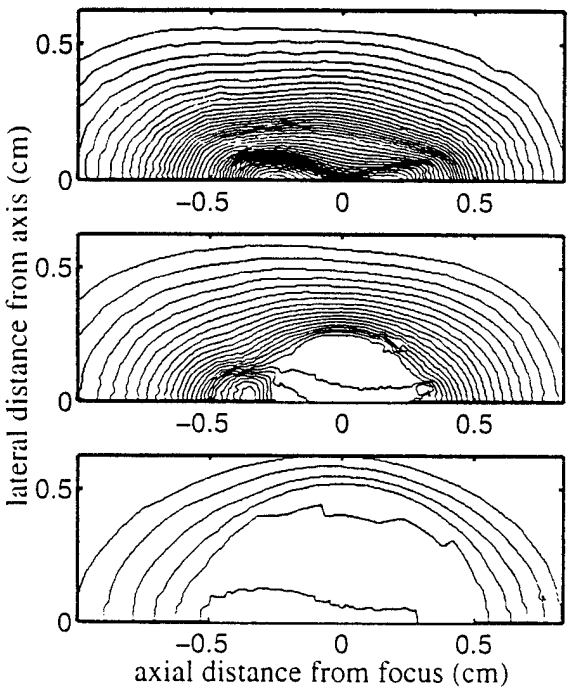

Figure 2: Contours of displacement in normal tissue (top, E=10kPa), in normal tissue with a 0.5 cm diameter lesion (middle, E=400kPa), and in normal tissue with a 1.0 cm diameter lesion (bottom, E=400kPa). The transducer is located on the left side of these images, and the profiles are symmetric about the x-axis. The location of the lesions is highlighted in gray. The lesions are moving toward the right as rigid bodies, with a smaller maximum displacement associated with the larger lesion.

and the Young's modulus (E) was 10 kPa. When lesions of varying stiffness were introduced, the Young's moduli ranged from 1 to 400 kPa, which is within the potential range of normal and diseased breast tissue [15, 5, 16]. The tissue was assumed to be elastic.

The equations of motion were then solved numerically using LS-DYNA (Livermore Software Technology Corporation, Livermore, CA). Radiation force was applied using a ramp and hold function, where the ramp up to the maximum force value was linear, occurring over 2 milliseconds, and the force was then applied continuously for 40 milliseconds. The same mesh was utilized for all simulations. Forces were applied to different mesh elements depending upon the transducer configuration, and tissue properties were applied to different elements depending upon the lesion size being modeled. There were 7440 elements in the mesh. The run times varied with Young's modulus, and were anywhere from 5 minutes to 6 hours on a 450 MHz Pentium PC.

In order to perform experimental validation of the model, it was also run using material properties corresponding to the calibration phantom (α=0.53 dB/cm/MHz, c=1550 m/s, E=0.3 kPa), and acoustic parameters corresponding to those in the experiment.

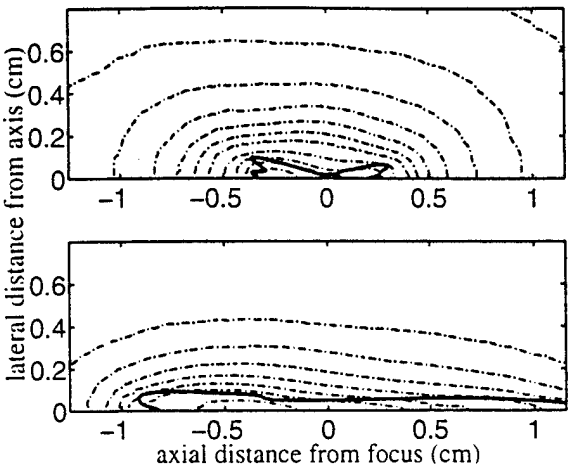

Figure 3: Magnified view of contours of displacement (dashed lines) in normal breast tissue (E=10kPa), for the F/1 (top) and F/3 transducer configurations (bottom). The transducer is on the left side of the page. The outer boundary of the associated radiation force field is superimposed on each figure as a solid black line. Each contour level represents a 10% decrease in displacement. Note that the shape of the displacement contours are similar to the shape of the radiation force fields: the F/1 contours are shifted slightly in front of the focus, but are fairly small, whereas the F/3 contours are much longer axially.

3. EXPERIMENTAL METHODS

Experiments were performed with a Siemens Elegra scanner (Siemens Medical Systems, Ultrasound Group, Issaquah, WA), that has been modified to allow user control of the acoustic beam sequences and intensities, as well as providing access to the raw Radio-Frequency (RF) data. The beam sequence was designed to transmit a series of 13 spatially distributed tracking beams, followed by 10 milliseconds of high intensity 'pushing' beams fired along a single line of flight in the center of the tracking beams, followed by another series of tracking beams interspersed with pushing beams (every other beam). This sequence was repeated for 100 milliseconds, and the raw RF data was stored for off-line processing. Experiments were performed in both an F/1 (more elements) and F/3 (fewer elements) focal configuration, using the same transmit parameters in both cases. Thus, in the calibrated phantom (F/3 configuration, α=0.53 dB/cm/MHz, c= 1550 m/s, and Young's modulus = 0.3 kPa), the derated spatial peak temporal average intensity was 1.0 W/cm^2, and the Mechanical Index was 0.3. In the lesion phantom (F/1 configuration, α=0.32 dB/cm/MHz, c=1550 m/s, Young's modulus = 0.05 kPa (tissue) and 13.5 kPa (lesion)), the derated spatial peak temporal average intensity was 2.9 W/cm^2, and the Mechanical Index was 0.6.

Off-line data processing was accomplished by performing cross-correlation between sequentially acquired tracking lines. Each tracking line was divided into a series of search regions, and the location of the peak in the cross correlation function between a kernel in the first tracking line and the corresponding search region in the next tracking line was used to estimate the tissue displacement in that region.

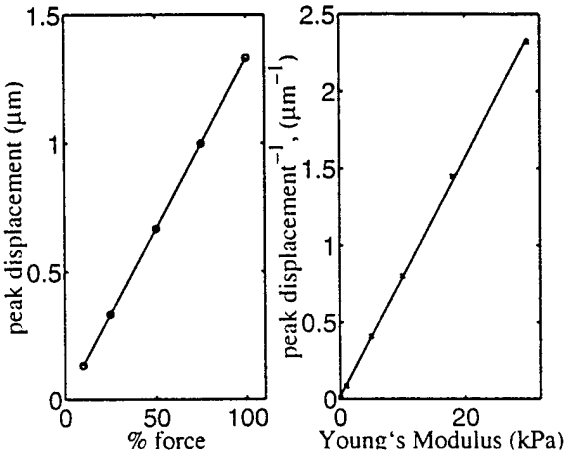

Figure 4: Simulated results for variations in force and stiffness. These portray a linear relationship between force and peak displacement, and an inverse relationship between stiffness and displacement.

4. RESULTS AND DISCUSSION

Figure 2 provides contours of constant displacement in the presence and absence of lesions of varying size generated using an F/1 transducer configuration. Considerable differences in displacement profiles exist in the presence and absence of the lesions. The peak displacement in the absence of the lesion is 1.2 μm, whereas for the 0.5 cm lesion the peak is 0.7μm, and for the 1.0 cm lesion it is 0.3μm. In addition, the lesions appear to exhibit rigid body motion, and thus the lateral extent of the displacement profiles is much larger in the presence of a lesion. The displacement profile in the absence of a lesion is much narrower, and is similar to the shape of the radiation force field (Fig. 3, top). Note that in the F/3 case (Fig. 3, bottom), the displacement profile is elongated axially, which results from the larger volume of the radiation force field.

The simulations were performed for varying forces and tissue stiffnesses (Figure 4). As expected, a linear relationship exists between peak displacement and force, and an inverse relationship is observed between tissue stiffness and peak displacement.

Excellent agreement is evident between the experimental and simulation results (Fig. 5). Both simulation and experiment portray a fairly elongated axial displacement pattern in the F/3 transducer configuration, with comparable lateral extent, resulting in teardrop-shaped profiles. In addition, the displacement magnitudes are similar (maximum displacements of 1.4 μm in the simulation, and 1.9 μm in the experiment, after 20 milliseconds of high intensity insonification).

Experiments were also performed in a phantom that was designed with an embedded 0.8 cm diameter lesion. This lesion was considerably more stiff than the surrounding tissue ($\sim$ 270 times). As predicted by the simulations, the displacement maps are different in the presence and absence of the lesion, both in magnitude and in shape, and the lesion appears to be moving as a rigid body. (Fig. 6). Note also that the axial extent of the displacement pattern in the absence of a lesion is much smaller in the F/1 case than in the F/3 case, as predicted by the simulations (Fig. 6, left and Fig. 5, right vs. Fig. 3)

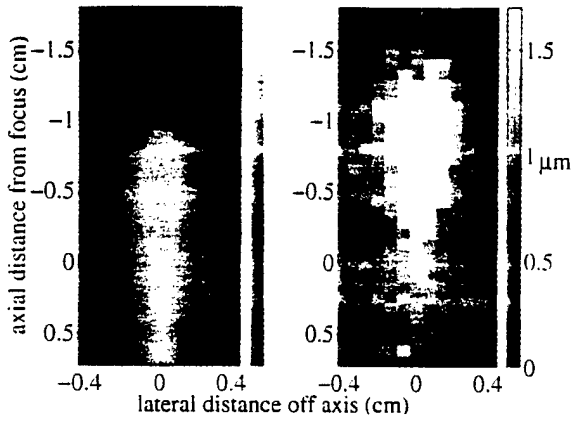

Figure 5: Simulated (left) and experimental(right) displacement maps for an F/3 transducer configuration in a homogeneous phantom (E=0.3kPa), after 20 milliseconds of high intensity insonification (*in situ* I_{spta}=1.0 W/cm^2, MI=0.3). The transducer is located at the top of these images. The shape of the displacement profiles is similar, although the location of the peak displacement is slightly closer to the transducer in the experimental case.

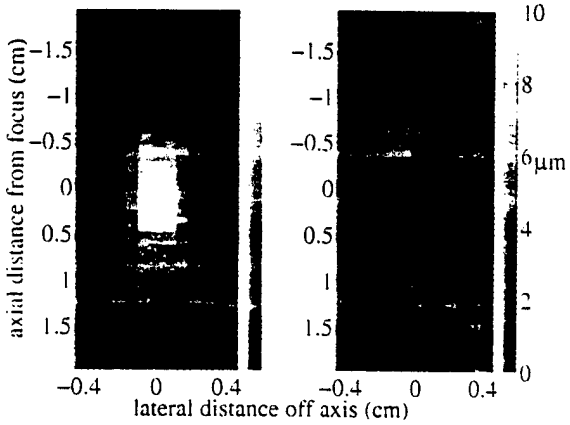

Figure 6: Experimental displacement maps after 20 milliseconds of focusing high intensity pulses (*in situ* I_{spta}=2.9 W/cm^2, MI=0.6) in a homogeneous region of the lesion phantom (left, E=0.05 kPa) and in the center of a 0.8 cm diameter lesion in the same phantom (right, lesion E=13 kPa). An F/1 focal configuration was used, with the transducer located at the top of the images.

The temporal response of the phantom was slightly slower than that predicted by the simulations (Fig. 7), which may be due to the assumption of an elastic medium in the simulations. Of particular interest is the fact that in the presence of a lesion, the response is much slower. Thus, after even 5 milliseconds of force application considerable differences in displacement profiles exist. The challenge is generating enough force to create detectable displacements (*i.e.* greater than 0.5 μm [21]) within 5 milliseconds.

The question of the maximum intensity output from diagnostic scanners is complex. Because the FDA limits are considerably lower than the maximum capacity of current diagnostic scanners, manufacturers do not quantify this parameter. The short temporal requirements are also an issue (only 5 milliseconds), because most system measurements are performed assuming a steady-state application. We conservatively estimate that for a clinically relevant range of tissue stiffnesses, the required temporal average intensity exceeds that currently available from diagnostic scanners by a factor of 30. However, when one considers the increase in radiation force associated with nonlinear propagation [14, 17, 8] (we have observed increases in radiation force by a factor of 2.6 in breast applications *in vivo* [8]), and the fact that two-dimensional transducers with more surface area will achieve higher intensities (simulations suggest a factor of 3), this factor drops to only 4.5.

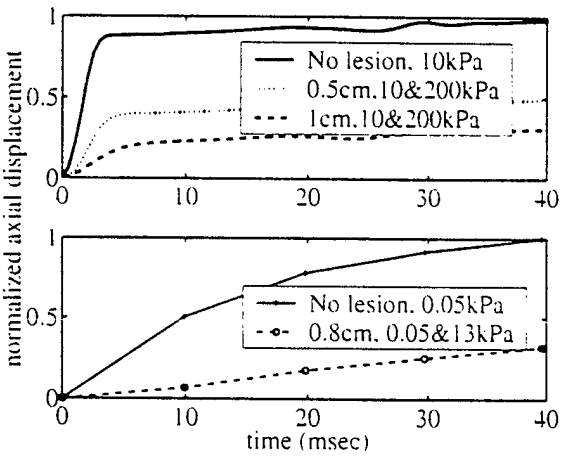

Figure 7: Simulated (top) and experimental (bottom) normalized displacement through time at the focal point of the transducer. The results are normalized to the displacement after 40 milliseconds in the no lesion case. The temporal response of the phantom is slightly slower than that predicted by the simulations.

5. CONCLUSIONS

The simulations and experiments presented herein provide the framework for the design of a Remote Palpation imaging system. For a clinically relevant range of elastic moduli and lesion sizes, considerably different displacement patterns were generated. The forces required to generate these displacements are higher than those currently used in diagnostic ultrasound. They should not pose a thermal danger to the patient due to their short duration, however, they may require the design of more efficient transducers. Most manufacturers are actively pursuing the development of diagnostic transducers capable of generating the required intensities. While further research is required to investigate the thermal and power issues, Remote Palpation as proposed herein appears to have clinical potential.

6. REFERENCES

[1] D. Dalecki. *Mechanisms of Interaction of Ultrasound and Lithotripter Fields with Cardiac and Neural Tissues.* PhD thesis, University of Rochester, 1993.

[2] M. Fatemi and J. Greenleaf. Ultrasound-stimulated vibro-acoustic spectrography. *Science*, 280:82–85, 1998.

[3] J. Jensen and N. Svendsen. Calculation of pressure fields from arbitrarily shaped, apodized, and excited ultrasound transducers. *IEEE UFFC*, 39:262–267, 1992.

[4] T. Krouskop, D. Dougherty, and S. Levinson. A pulsed doppler ultrasonic system for making noninvasive measurements of the mechanical properties of soft tissue. *J. Rehabil. Res. Dev.*, 24:1–8, 1987.

[5] T. Krouskop, T. Wheeler, F. Kallel, B. Garra, and T. Hall. Elastic moduli of breast and prostate tissues under compression. *Ultrasonic Imaging*, 20:260–274, 1998.

[6] R. Lerner, S. Huang, and K. Parker. Sonoelasticity images derived from ultrasound signals in mechanically vibrated tissues. *UMB*, 16:231–239, 1990.

[7] S. Levinson. Ultrasound propagation in anisotropic soft tissues, the application of linear elastic theory. *J. Biomech.*, 20:251–260, 1987.

[8] K. Nightingale, P. Kornguth, and G. Trahey. The use of acoustic streaming in breast lesion diagnosis: a clinical study. *UMB*, 25(1):75–87, 1999.

[9] K. Nightingale, R. Nightingale, T. Hall, and G. Trahey. The use of radiation force induced tissue displacements to image stiffness: a feasibility study. 23rd International Symposium on Ultrasonic Imaging and Tissue Characterization, May 27-29, 1998.

[10] W. Nyborg. Acoustic streaming. In W. Mason, editor, *Physical Acoustics*, volume IIB, chapter 11, pages 265–331. Academic Press Inc, New York, 1965.

[11] M. O'Donnell, A. Skovoroda, B. Shapo, and S. Emelianov. Internal displacement and strain imaging using ultrasonic speckle tracking. *IEEE UFFC*, 41:314–325, 1994.

[12] J. Ophir, I. Cespedes, H. Ponnekanti, Y. Yazdi, and X. Li. Elastography: A quantitative method for imaging the elasticity of biological tissues. *Ultrasonic Imaging*, 13:111–134, 1991.

[13] K. Parker, S. Huang, R. Musulin, and R. Lerner. Tissue response to mechanical vibrations for sonoelasticity imaging. *UMB*, 16:241–246, 1990.

[14] A. Sarvazyan, O. Rudenko, S. Swanson, J. Fowlkes, and S. Emelianov. Shear wave elasticity imaging: A new ultrasonic technology of medical diagnostics. *UMB*, 24(9):1419–1435, 1998.

[15] A. Sarvazyan, A. Skovoroda, S. Emelianov, J. Fowlkes, J. Pipe, R. Adler, R. Buxton, and P. Carson. Biophysical bases of elasticity imaging. *Acoustical Imaging*, 21:223–240, 1995.

[16] A. Skovoroda, A. Klishko, D. Gusakyan, Y. Mayevskii, V. Yermilova, G. Oranskaya, and A. Sarvazyan. Quantitative analysis of the mechanical characteristics of pathologically changed soft biological tissues. *Biophysics*, 40(6):1359–1364, 1995.

[17] H. Starritt, F. Duck, and V. Humphrey. Forces acting in the direction of propagation in pulsed ultrasound fields. *Phys. Med. Biol.*, 36:1465–1474, 1991.

[18] T. Sugimoto, S. Ueha, and K. Itoh. Tissue hardness measurement using the radiation force of focused ultrasound. In *Proceedings of the 1990 Ultrasonics Symposium*, pages 1377–1380, 1990.

[19] G. Torr. The acoustic radiation force. *Am. J. Phys.*, 52:402–408, 1984.

[20] W. Walker. Internal deformation of a uniform elastic solid by acoustic radiation force. *JASA*, 105(4):2508–2518, 1999.

[21] W. Walker and G. Trahey. A fundamental limit on delay estimation using partially correlated speckle signals. *IEEE UFFC*, 42(2):301–308, 1995.

[22] Y. Yamakoshi, J. Sato, and T. Sato. Ultrasonic imaging of internal vibration of soft tissue under forced vibration. *IEEE UFFC*, 17(2):45–53, 1990.

10.2 Experimental Implementation Paper

On the feasibility of remote palpation using acoustic radiation force

Kathryn R. Nightingale, Mark L. Palmeri, Roger W. Nightingale, and Gregg E. Trahey

Duke University, Department of Biomedical Engineering, Box 90281, Durham, NC 27708

Received:

Running Title: Remote Palpation

PACS numbers: 87.63.Df, 43.80.Qf, 43.80.Sh, 87.50.Kk, 43.80.Vj

Submitted to: JASA

Abstract

A method of acoustic Remote Palpation, capable of imaging local variations in the mechanical properties of tissue, is under investigation. In this method, focused ultrasound is used to apply localized (on the order of 2 mm^3) radiation force within tissue, and the resulting tissue displacements are mapped using ultrasonic correlation based methods. The tissue displacements are inversely proportional to the stiffness of the tissue, and thus a stiffer region of tissue exhibits smaller displacements than a more compliant region. A small volume of tissue that is significantly stiffer than the surrounding medium (i.e. a lesion) tends to exhibit rigid body motion. In this paper, the feasibility of Remote Palpation is demonstrated experimentally using breast tissue phantoms with spherical lesion inclusions, and *in vitro* liver samples. A single diagnostic transducer and modified ultrasonic imaging system are used to perform Remote Palpation. The displacement images are directly correlated to local variations in tissue stiffness with higher contrast than the corresponding B-mode images of the phantoms. Relationships between acoustic beam parameters, lesion characteristics and radiation force induced tissue displacement patterns are investigated and discussed. The results show promise for the clinical implementation of Remote Palpation.

I. INTRODUCTION

A. The Remote Palpation Method

It is hypothesized that acoustic radiation force can be used to generate localized tissue displacements, and that these displacements will be directly correlated with localized variations in tissue stiffness. It is further hypothesized that this can be accomplished using a single transducer on a diagnostic ultrasound scanner to both generate the radiation

force and detect the resulting displacements. These hypotheses form the basis for a new imaging method called Remote Palpation. In this method, acoustic radiation force is used to generate localized displacements in tissue. These displacements are measured using ultrasonic correlation based methods. The magnitude of the tissue displacement is inversely proportional to the local stiffness of the tissue. A volume of tissue that is significantly stiffer than the surrounding tissue (*i.e.* a breast lesion) tends toward rigid body motion, and thus distributes the localized force throughout the surrounding tissue. The volume of displaced tissue is larger, and the maximum displacement smaller than that for normal tissue. Radiation force induced displacement maps are generated at multiple locations, and combined to form a single image of variations in tissue stiffness throughout an extended Field of View (FOV). A single transducer on a diagnostic scanner is used to both generate the high intensity 'pushing' beams and track the resulting tissue displacements.

B. Purpose

Two potential clinical applications for Remote Palpation are lesion detection and characterization, and the identification and characterization of atherosclerosis. This paper focuses on the former, as it pertains to the early detection of breast cancer, which has been shown to significantly improve patient survival. Existing methods of breast cancer detection include screening mammography and palpation, either by patient self-examination or clinical breast exam. Palpation relies on the manual detection of differences in tissue stiffness between breast lesions and normal breast tissue. The success of palpation is due to the fact that the elastic modulus (or Young's modulus) of breast lesions is often an order of magnitude greater than that of normal breast tissue[1,2], *i.e.* breast lesions feel 'hard' or 'lumpy' as compared to normal breast tissue.

Differences in Young's moduli are the basis for the investigation of imaging modalities that provide information about the stiffness of tissue. Traditionally, these have fallen into two categories: 1) Sonoelasticity, in which low frequency shear wave propagation is imaged

using Doppler or Magnetic Resonance methods. Estimates of the Elastic modulus (Young's modulus) of the tissue are based upon this information[3–7]. 2) Elastography, in which local variations in tissue strain are determined by measuring local displacements that occur during global tissue compression. Estimates of Elastic Modulus are based upon reconstruction methods to determine the elastic moduli associated with the measured strain fields. [1,8–11]. Remote Palpation is similar to elastography, which has recently demonstrated some success in the detection of malignant breast lesions[12], however it has several potential advantages. These include the very localized application of radiation force (as opposed to global external compression), the decrease in maximum tissue strain required for lesion visualization, and the potential for real-time implementation without the need for external compression fixtures.

II. BACKGROUND

A. Acoustic Radiation Force

Acoustic radiation force is a unidirectional force that is applied to absorbing or reflecting targets in the propagation path of an acoustic wave. This phenomenon is caused by a transfer of momentum from the acoustic wave to the propagation medium. The contribution of absorption is in the direction of wave propagation, whereas the contribution of scattering is dependent upon the angular scattering properties of the target. In the event that the target is both absorbing and has a scatterer that acts as a reflector with an axis of symmetry perpendicular to the direction of wave propagation (*e.g.* the reflecting target is spherical), the radiation force is entirely in the direction of wave propagation. In this situation, the radiation force is given by[13]:

$$F = \left(\Pi_a + \Pi_s - \int \gamma \cos\theta r dr d\theta\right) \langle E \rangle \,, \tag{1}$$

where Π_a is the total power absorbed by the target, Π_s is the total power scattered by the target, γ is the magnitude of the scattered intensity, θ is the scattering angle, $rdrd\theta$ is an

area element of the projection of the target onto the axial/lateral plane, and $\langle E \rangle$ is the temporal average energy density of the propagating acoustic wave.

If there is no absorption, and the target is perfectly reflecting (*i.e.* $\theta = 180°$), the integral term becomes $-\Pi_s$ and the total radiation force is $\{2\Pi_s \langle E \rangle\}$. The factor of 2 can be intuitively explained by the fact that the target stops the wave from propagating, and reflects it in the opposite direction[14]. If the target is a Rayleigh scatterer (*i.e.* its diameter is much smaller than a wavelength), scattering occurs in all directions equally, and the integral term is zero. Thus the total radiation force on the scatterer is $\{(\Pi_a + \Pi_s) \langle E \rangle\}$.

For a tissue model comprised of a collection of Rayleigh scatterers, one can sum the contribution of the radiation force from each scatterer to determine the total force due to scattering. However, in tissue, the majority of the attenuation of an acoustic wave is due to absorption[15], thus the contribution to the radiation force by scattering in soft tissue can, in general, be neglected. Eq. 1 then becomes:

$$F = \Pi_a \langle E \rangle . \tag{2}$$

Assuming plane wave propagation, the radiation force applied to tissue is thus [14,16–18]:

$$F = \frac{2\alpha I}{c}, \tag{3}$$

where F (which is in the form of a body force, or force per unit volume) is the acoustic radiation force [kg/(s^{2}cm^2)], or [dynes/(1000 cm^3)], c [m/s] is the speed of sound in the medium, α [m^{-1}] is the absorption coefficient of the tissue, and I [Watts/cm^2] is the temporal average intensity of the acoustic beam at a given point in the tissue. For a focused acoustic beam propagating through soft tissue, the 'target' is the tissue, and the force is applied throughout the focal region of the acoustic beam.

An important phenomenon that is not modeled by Equation 3 is the enhancement of radiation force generated by nonlinear propagation of an acoustic wave[19,18,20,21]. For the same temporal average intensity, a wave with higher pressure amplitude and shorter pulse duration generates a larger radiation force than does a lower amplitude, longer duration wave. This

is due to the higher order harmonics generated by nonlinear propagation, which result in an increase in absorption[19,18,20,21]. Nonlinear propagation also narrows the transmit beam and shifts the intensity field of a focused acoustic beam[20]. Increases in radiation force resulting from nonlinear enhancement by a factor of 2.6 have been observed in breast applications *in vivo*[22]. These effects can be modeled using Equation 4, where the contribution to radiation force of each harmonic component (n) of the acoustic wave can be computed at every point in the focal region of the acoustic beam [21,18]:

$$F = \frac{2}{c} \sum_n \alpha_n I_n. \tag{4}$$

The potential applications of acoustic radiation force in diagnostic imaging have heretofore been widely ignored, primarily because the available energy from diagnostic ultrasound systems was low. However, advances in transducer and system design in recent years have resulted in considerable increases in the maximum possible acoustic energy output from these systems. This has sparked a renewed interest by several laboratories in the potential applications of acoustic radiation force. Our laboratory demonstrated the use of acoustic radiation force to induce acoustic streaming in cyst fluid, and thus differentiate fluid-filled from solid breast lesions *in vivo*[22,23]. Several authors have proposed the use of acoustic radiation force to remotely characterize the mechanical properties of tissue [19,24–27]. One application involves the use of a radiation force field oscillating at the beat frequency of two confocal transducers to vibrate an object; the vibrations are detected by a hydrophone, and are used to generate an image[27]. In another application, acoustic radiation force is used to displace tissue, and the speed of the shear waves generated immediately after force removal is monitored to characterize variations in tissue Young's modulus[19]. In yet another application, acoustic radiation force is used to manipulate the vitreous humor of the eye[24].

B. Tissue Response to Radiation Force

Remote Palpation applies localized forces to tissue, which can be described for idealized cases by elasticity theory. For an infinitely small distributed force volume, the strain field

can be derived from the analytic solution for a point load in an infinite elastic solid[28]:

$$\epsilon_z = \frac{-(P\,z\,(1+\nu)\,(4\,z^2\,(-1+\nu)+r^2\,(-1+4\,\nu)))}{8\,E\,\pi\,(r^2+z^2)^{\frac{5}{2}}\,(-1+\nu)}, \tag{5}$$

$$\epsilon_r = \frac{-(P\,z\,(-2\,r^2+z^2)\,(1+\nu))}{8\,E\,\pi\,(r^2+z^2)^{\frac{5}{2}}\,(-1+\nu)}, \epsilon_\theta = \frac{-(P\,z\,(1+\nu))}{8\,E\,\pi\,(r^2+z^2)^{\frac{3}{2}}\,(-1+\nu)},$$

where $\epsilon_{z,r,\theta}$ are the 3 dimensional normal strains. The variable z is the axial distance along the line-of-action of the applied force, P is the magnitude of the applied force, r is the radial distance from the point of applied force, E is the Young's modulus of the material, and ν is Poisson's ratio. The displacement of the material in the direction of the applied force is obtained by integration of ϵ_z[28]:

$$w = \frac{P\,(1+\nu)\,(4\,z^2\,(-1+\nu)+r^2\,(-3+4\,\nu))}{8\,E\,\pi\,(r^2+z^2)^{\frac{3}{2}}\,(-1+\nu)} \tag{6}$$

Solving these equations for a magnitude of force similar to that used in RP (*i.e.* $P = 0.01$ dynes, $\nu = 0.49$, $E = 30{,}000$ dynes/cm^2 (3.0 kPa)) gives an estimate of the size of the associated displacement and strain fields. The solution indicates that the spatial extent of the axial strain field is very small, with strains decreasing to a negligible amount at a distance of 0.2 mm from the loading point. Strains in the radial and circumferential directions are even smaller. This implies that lesions that are separated by more than 0.4 mm can be differentiated when excited with point loads at a 0.2 mm spacing.

Several insights can be gained from this simplified analysis. First, RP can locally sample tissue stiffness with minimal confounding artifacts from neighboring tissue stiffness variations (*i.e.* two lesions in close proximity will not affect each other). Second, given that the strain and displacement fields are highly localized, displacements measured at the point of force application will be highly correlated with tissue stiffness at that location. Thus, for a local increase in tissue stiffness, smaller displacements will occur than in the surrounding tissue.

C. High Intensity Acoustic Beams

Potential risks associated with Remote Palpation arise from the fact that high intensity acoustic pulses are utilized. The FDA provides two indices to monitor the safety of diagnostic ultrasound. The Mechanical Index (MI) is indicative of the potential for cavitation, and the Thermal Index (TI) is indicative of the potential temperature rise. The high intensity pulses used in Remote Palpation will not exceed the MI limit of 1.9[29], thus cavitation is not anticipated (primarily because of the relatively high frequencies (7 to 14 MHz)). Nor is it anticipated that the TI will exceed 6, which is the limit above which the FDA requires special provisions for approval of use. Finite element models of the heating associated with the high intensity beams used for Remote Palpation indicate that the temperature rise will be less than 1°C[30], which would correspond to a TI of 1.

Throughout this paper, the derated (or *in situ* estimated) spatial peak temporal average intensity for the different acoustic beams is provided in order to calibrate the reader. The FDA currently limits the spatial peak temporal average intensity ($I_{spta.3}$) to 0.72 W/cm^2 *in situ*[29], which is intended as an indirect indicator of potential tissue heating. However, this limit was determined assuming an indefinite application time. Short duration, high intensity acoustic pulses as are used in Remote Palpation (*i.e.* 10 milliseconds) were not foreseen in the development of this FDA limit, and thus the TI and/or temperature increase estimates provide a more appropriate indication of the potential for thermal effects.

D. Goals

The goals of the work presented herein are: first, to experimentally demonstrate the feasibility of Remote Palpation imaging; second, to determine whether the displacement images generated during Remote Palpation imaging are directly correlated with variations in tissue stiffness; and third, to determine whether a single transducer on a diagnostic scanner can be used to perform Remote Palpation imaging.

III. METHODS

Experiments were performed with a Siemens Elegra scanner (Siemens Medical Systems, Ultrasound Group, Issaquah, WA), that has been modified to allow user control of the acoustic beam sequences and intensities, as well as providing access to the raw Radio-Frequency (RF) data. A Siemens 75L40 linear array was used for these experiments. Figure 2 provides a schematic of a typical linear array, and defines the different dimensions discussed below. The 75L40 array consists of 194 elements, each of which are 5 mm tall and approximately 0.2 mm wide, with a center frequency of 7.2 MHz. The number of active elements can be selected electronically to adjust the lateral transmit aperture width. There is a fixed-focus acoustic lens on each element that focuses in the elevation dimension. Lateral focusing is accomplished electronically by applying the appropriate delays to each active element (Fig. 2). Interrogation of different spatial locations is accomplished by using different sub-apertures (or groups of elements) within the array. In all of these experiments, the lateral aperture was considerably larger than the elevation aperture. This resulted in an asymmetric focal region that was more tightly focused in the lateral dimension than in the elevation dimension (in contrast to a piston, which has an axi-symmetric focal region).

The tracking beams were standard diagnostic B-mode pulses (*i.e.* single cycle pulses, F/1 focal configuration, apodized, $I_{spta} < 0.1 W/cm^2, MI \sim 0.4$). The pulse length, transmit voltage, and transmit F-number (i.e. number of active transmit elements) of the beams were varied in the experiments. The pulse lengths ranged from 0.8 to 5.8 μsec, the transmit voltages ranged from 30 to 140 volts (in contrast to 20 volts for the tracking beams), the F-numbers ranged from F/1 to F/3, the Pulse Repetition Frequencies (PRFs) were varied from 3 to 10 kHz, and they were not apodized.

Several beam sequences were designed to investigate the temporal and spatial response of the phantoms. The experiments are divided into three groups: single pushing location with 2-D tracking region, single A-line interrogation, and multiple pushing locations.

A. Single pushing location with 2-D tracking region

For these experiments, the transducer was held in a stationary location. The pulse sequence was designed to transmit a series of 13 spatially distributed tracking beams (*i.e.* B-mode interrogation using 13 laterally spaced lines, Fig. 3, top) at a PRF of 3584 Hz. This was followed by 10 milliseconds of pushing beams fired at a PRF of 3584 Hz along a single line of flight in the center of the tracking beams, followed by another series of tracking beams interspersed with pushing beams (every other beam, see Fig. 3). The spacing of the tracking beams was 0.7 mm. This sequence was repeated for 50 milliseconds. The raw RF data was stored for off-line processing.

B. Single A-line interrogation

This sequence was designed to fire all of the tracking beams in the same spatial location as the pushing beams (*i.e.* A-line interrogation, Fig. 3, bottom). The Pulse Repetition Frequency (PRF) for these experiments was 10240 Hz. Every other beam was a tracking beam, thus the PRF for the tracking beams was 5120 Hz. The PRF of the pushing beams was varied by firing either every pushing pulse (PRF 5120 Hz, as shown in Fig. 3, bottom), every fourth pushing pulse (PRF 1280 Hz), every fifth pushing pulse (PRF 1024 Hz), or every sixth pushing pulse (PRF 853 Hz). The first beam fired was always a tracking beam which served as a reference for the initial position. The raw, Radio-Frequency (RF) data was stored and processed off-line.

C. Multiple pushing locations with 2-D tracking regions

These sequences were the same as those described in Section III A, however only 11 tracking lines were utilized for each pushing location (instead of 13), and these lines were spaced at 0.09 mm. This resulted in datasets from each pushing location covering +/- 0.5 mm laterally. Multiple pushing locations were interrogated by connecting the transducer

to an automated translation stage, and translating the transducer to interrogate different regions of tissue (using the same acoustic beam parameters and sequences at each location). These experiments were performed on two different phantoms, each with an 8 mm diameter lesion located 1.0 cm from the surface of the phantom. The phantoms were submerged in a liquid slurry phantom material, that was created by blending a homogeneous phantom. This was done in order to achieve the same absorption and attenuation of the beam for each axial transducer position, without applying compression to the phantom itself. The pushing point locations spanned 11 mm laterally, and 9 mm axially with 1 mm spacing in both dimensions (Fig. 8 top). The raw RF data from each pushing location was stored for off-line processing.

D. Data Processing

Off-line data processing was accomplished by performing cross-correlation between sequentially acquired tracking lines[31,9]. Each tracking line was divided into a series of search regions, and the location of the peak in the cross correlation function between a kernel in the first tracking line and the corresponding search region in the next tracking line was used to estimate the tissue displacement in that region. One-wavelength translations were removed and all displacements associated with a correlation coefficient greater than 0.99 were considered valid.

E. Intensity measurements

Pressure and intensity calibration measurements were made in accordance with the guidelines provided by the American Institute of Ultrasound in Medicine [32]. These measurements are complicated at higher transmit voltages due to acoustic saturation[33]. Saturation occurs at lower pressures in water than it does in phantoms and tissue, thus accurate measurement of the intensities and pressures used for the highest transmit voltages was not possible. However, the relationship between acoustic radiation force and the resulting displacement

is linear[26]. Therefore, one can obtain an estimate of the magnitude of the radiation force generated by a very high intensity acoustic beam by comparing the corresponding peak displacement obtained in the same phantom using a lower intensity, quantifiable beam. Where Eq. 3 applies, the ratio of the forces is equal to the ratio of the intensities. Thus one can obtain an estimate of the intensity in the higher energy beam under the assumption of linear propagation by evaluating the ratio of the peak displacements.

The above approach does not account for the enhancement in radiation force caused by nonlinear propagation[20,19,18,22]. This results in an overestimate of the intensity of the beam, due to the assumption of a single frequency and absorption coefficient in Eq. 3. Even so, this method provides a reasonable approximation of the intensities, and thus is utilized to estimate the intensities used in the experiments where actual measurements were not possible (*i.e.* transmit voltages of 80 volts and higher).

F. Phantom Construction

Experiments were performed both in elastography phantoms, and in thawed, de-veined calf liver. The elastography phantoms were fabricated from gelatin, graphite, alcohol, water, and glutaraldehyde[34]. The lesions in the phantoms were all generated from a single batch, with a recipe corresponding to a higher Young's Modulus than the background material. Table I provides the recipes for the phantoms. The calf liver was purchased from the local grocery store, frozen, in a vacuum-sealed package. It was thawed under water, and the experiments were performed on the same day.

G. Phantom Mechanical Property Characterization

Characterization of the Young's modulus of tissue and tissue-like media is very challenging. Only a few reports exist in the literature on the subject[35,36,2]. The reported values vary considerably, possibly because Krouskop et. al. applied pre-compression while making their measurements, whereas the other groups did not[35,36,2], and the stiffness of tissue increases

with compression[2]. The numbers provided here were obtained in a method consistent with those reported. This involved modeling of the test apparatus to account for boundary condition deviations from the assumed theoretical solution, and comparison of the experimental measurements with both the theoretical model (which had inherent assumptions) and the boundary condition correction model[34,36]. A thorough description of these methods is outside of the scope of this paper. It is possible that our measurements suffer from a constant offset, however, the relative stiffnesses of the phantoms are consistent (*i.e.* in order from the most compliant to the most stiff: Phantom C, Phantom A, Phantom B, Lesion Material, Phantom D).

IV. RESULTS

A. Phantom Fabrication

Phantoms A, B, and C were designed using the same recipe shown in Table I. Phantom A had an 11 mm diameter lesion, Phantoms B and C each had an 8 mm diameter lesion. Although the ingredients were the same for each of these phantoms, the background material varied in its Young's modulus slightly between batches. This is likely due to limited control of temperature fluctuations during fabrication.

The measured Young's modulus of the lesion material was 0.5 kPa. The Young's modulus of the background material in Phantoms A, B and C was 0.07 kPa, 0.13 kPa, and .05, respectively. These values are approximately an order of magnitude lower than those reported for soft tissue[35,36], however the Lesion to Tissue Stiffness Ratios (LTSR) are between 3.8 and 10, which are consistent with LTSRs reported for breast tissue[35].

The Young's modulus of Phantom D was 1.6 kPa. Phantom D was designed without a lesion. The Young's modulus of the liver sample used for the experiments was not measured, however reported values in the literature range from 0.4 to 1.7 kPa[36]. Comparison of the steady state displacements generated with the same Remote Palpation imaging sequence in

both Phantom D and the liver sample indicate that Phantom D was approximately 4 times more stiff than the liver sample.

B. Single pushing location with 2-D tracking region

Fig. 4a portrays the two-dimensional displacement profile generated in a homogeneous portion of Phantom A for an F/1 focal configuration with a lateral focal point of 20 mm, and a relatively low transmit voltage (29 volts). This image was generated after 10 milliseconds of force application, and represents the tissue displacement profile (in two dimensions) resulting from a single force application. If the acoustic beam had generated a point load, one would expect a small circular displacement profile, consistent with Fig. 1. However, the focused acoustic beam used for these experiments is associated with an intensity field that is approximately the size of its focal region. The extent of the inner contour (-2dB) shown in Fig. 4a is approximately the size of the intensity field of the acoustic beam (including intensity values down to -20 dB).

The derated spatial peak temporal average intensity of the pushing beams used to generate Fig. 4a was 2.4 W/cm^2, and the associated radiation force, as computed using Eq. 3, was 100 dynes/cm^3. The maximum displacement is 2.9 microns. Fig. 4b shows the two-dimensional displacement profile generated when the same beam sequence is focused in the center of an 11 mm diameter lesion in the same phantom. The maximum displacement is smaller than in the homogeneous case (1.4 microns), and the shape of the intensity field is not apparent in the contours of displacement.

Fig. 4c portrays the displacement map with the pushing beams focused in the same phantom location as in Fig. 4a, however with a much higher transmit voltage (80 volts). The shape of the contours of displacement are similar to Fig. 4a, however they are shorter axially, and the peak has shifted slightly closer to the transducer. The estimated *in situ* peak intensity ($I_spta.3$) of this beam is 15 W/cm^2 (Section III E). The maximum displacement is 18 microns.

Fig. 4d was obtained using the same beam sequence as in Fig. 4c, but focused within the lesion (in the same location as in Fig. 4b). The maximum displacement is 7 microns. Comparison of plot pairs a-b and c-d indicates that their differences are similar. In both plot pairs, the -10 dB contours begin axially in similar locations. As predicted, the presence of the lesion decreases the peak displacement, and alters the displacement profile from the homogeneous case. In both Fig. 4b and Fig. 4d the maximum displacement is approximately half of that in the corresponding homogeneous cases (Fig. 4a and Fig. 4c).

Fig. 5 portrays the displacement profiles generated in the calf liver sample, using different focal positions (10, 15, and 20 mm). In each case, an F/1 focal configuration was maintained (*i.e.* the number of active transmit elements was increased as the focal position depth increased). The estimated derated peak intensity of the beam used for the 20 mm focus is 120 W/cm^2 (Section III E). In each plot, the peak in the displacement profile occurs slightly in front of the focal position. Although the focal configuration was constant (F/1), the maximum displacement differs in each plot: 12, 11 and 16 microns, for plots a, b, and c respectively.

C. Single A-line interrogation

Fig. 6 portrays the maximum displacement through time in Phantom A. In this sequence, all of the tracking lines were fired along the same line (spatially) as the pushing lines, and the tracking and pushing lines were interspersed (*i.e.* track, push, track, push). The system was in an F/1 focal configuration, and the transmit voltage was 140 volts.

The curves in the top plot were generated using the same PRF for both the pushing and tracking pulses (3584 Hz), but different pulse lengths. As expected, the increase in steady state displacement is linearly related to the increase in pulse length (*i.e.* the increase in intensity). For example, the steady state displacement for the 3.4 microsecond pulse is double that of the 1.7 microsecond pulse. Also as expected, the time constants for displacement were similar for the different pulse lengths ($\sim$6 milliseconds, determined by fitting the curves

to an exponential).

The bottom plot was generated using pushing beams with the same pulse length and transmit voltage, but with different PRFs (the PRF of the tracking beams was held constant at 3584 Hz). The frequency of the 'rectified sine wave' apparent in each of the three curves corresponds to the PRF of the high intensity beams for each experiment. This temporal response is due to the relaxation of the tissue between pushing beams. Note that the magnitude of the relaxation increases with increasing mean tissue displacement. This relaxation is not apparent in the top plot because the PRF of the tracking beams was the same as that for the pushing beams, thus the relaxation response was undersampled. Again, as expected, the time constant for each of these curves was similar to those in the top plot ($\sim$6 milliseconds).

Fig. 7 portrays the temporal response of Phantoms A, D, and the liver sample during force application and after removal of the force. The ramp-down time constants are 4.2, 1.5, and 7.9 milliseconds, respectively. This parameter is indicative of the damping present in the tissue. The ramp-up time for Phantom D is about the same (1.6 milliseconds), however it is slightly faster for both Phantom A (5.1 milliseconds), and the liver sample (6.2 milliseconds).

D. Multiple pushing locations with 2-D tracking regions

Fig. 8(top) provides a schematic showing the position of the different pushing locations (*i.e.* focal points) used in the multiple pushing location experiments, and their relationship to the lesion in Phantom C. The sub-plots show the displacement in the same spatial location as the pushing beam after 10 milliseconds of force application in each grid location. Each subplot represents the displacements obtained at all of the axial positions in one lateral location in the grid (as indicated by the letters a-f). The presence of the lesion is clear in these plots, where a 'dip' in the axial profile occurs in each lateral location that intersected the lesion. The extent of the 'dip' corresponds to the length of the interrogated cross-section of the lesion.

Fig. 9a portrays the combination of all of the displacement data from the different pushing

locations (from Fig. 8) into a single displacement image. In this image, the displacement at each pixel is determined by computing the average displacement from all of the pushing locations whose focal regions overlap with that pixel. The lesion is clearly apparent in the displacement image, while it is not as evident in the conventional B-mode image (Fig. 9b).

Fig. 10a represents a combined displacement image of Phantom B that was generated in the same way as Fig. 9a. Phantom B had a slight tear along the interface between the lesion and the background on the left side of the image. This region filled with the liquid slurry phantom material that surrounded the phantom. Therefore, it was much more compliant than the phantom itself. This is clearly apparent in the displacement map shown in Fig. 10a, as well as in the corresponding B-mode image (Fig. 10b).

V. DISCUSSION

Several insights can be gained from the simplified point load analysis of radiation force presented in the background section (Fig. 1). Most significantly, the limited spatial extent of the force leads to two advantages: 1) Remote Palpation can locally sample tissue stiffness with minimal confounding artifacts from neighboring tissue stiffness variations. This is in contrast to elastography, where a stiff or soft inclusion impacts the strain field up to 2 diameters away[37]. 2) Given that the strain and displacement fields are highly localized, displacements measured at the point of force application are highly correlated with tissue stiffness at that location. For a local increase in tissue stiffness, smaller displacements occur than in the surrounding tissue. Thus, the Remote Palpation method provides the ability to generate high resolution maps of tissue displacement that are directly correlated with local variations in tissue stiffness (Figs. 9 and 10).

Figures 9 and 10 clearly demonstrate the feasibility of acoustic Remote Palpation imaging. The homogeneous background medium is a fairly uniform gray color, and the stiffer lesion is clearly apparent as a darker region. The spatial extent of the lesions shown in these images is comparable to that in the corresponding B-mode images. The presence of

the lesion is not apparent in the displacement maps beyond the lesion boundaries. This is clearly evident in Fig. 8, where the displacements on either side of the 'dip' are very similar to those obtained in the same axial location in the absence of a lesion (*e.g.* subplots 8d and 8f). This supports the hypotheses that Remote Palpation imaging can be performed in complex media without suffering from artifacts from neighboring structures, and that the displacements achieved in Remote Palpation imaging are directly correlated to tissue stiffness.

As predicted by finite element simulations[26], the displacement profiles remain approximately the same shape for increases in intensity; and the displacement magnitude scales with intensity (Fig. 4a,c). The slight decrease in axial extent of the displacement profile, and the slight shift of the displacement peak towards the transducer is likely a result of nonlinear propagation of the higher pressure amplitude acoustic beam [20,38]. In both cases, the presence of the lesion results in a considerably different displacement profile, and it appears to move as a rigid body in the high intensity case. The ratio of the displacement at the focal point in the presence/absence of the lesion for the low intensity case is 2.3 (Fig. 4a,b); and for the high intensity case this ratio is 2.6 (Fig. 4c,d). Previously presented finite element simulations suggest that these numbers should be the same [26], however, these simulations did not account for nonlinear propagation. It is possible that the lesion and the background medium have slight differences in nonlinearity, which could account for the slightly larger ratio in the high intensity case.

In comparing Figs. 4a and c, and Figs. 4b and d, it is clear that the images generated at lower intensities exhibit more noise. This is due to the lower displacements in these images. The minimum detectable displacement for a correlation based tracking algorithm is dependent upon several factors: system Signal-to-Noise Ratio (SNR), pulse-to-pulse correlation, signal bandwidth, as well as the center frequency and pulse length of the tracking beams. Utilizing values for the above parameters that are applicable to the experiments performed herein (*i.e.* 40 dB, 0.99, 70%, 7.2 MHz, 0.3μsec, respectively), the lower limit of displacement that can be tracked is computed to be to be 0.5μm[39]. The majority of the displacements

in the low intensity cases (Figs. 4a and b) are close to this minimum detectable value, thus these displacement images have a lower Signal-to-Noise ratio (SNR) than the higher intensity images (Figs. 4c and d). Clearly, larger displacements are preferable to achieve better SNRs.

Figure 5 represents the first *in vitro* Remote Palpation displacement maps generated in a tissue sample. The varying lateral focal point experiments were performed in order to investigate the limitations presented by a linear array with a fixed elevation focus. Each of the three maps was generated using an F/1 focal configuration and the same transmit voltage and pulse length. If the arrays were axi-symmetric (*i.e.* pistons), one would expect identically shaped displacement profiles, with decreases in peak displacement at deeper focal positions due to the attenuation of the overlaying tissue. However, because a linear array (asymmetric, 5 mm x 20 mm) was used, the peak displacement actually occurs for the deepest focal position (Fig. 5c). This focal position is closer to the elevational focal point than the other two focal positions, which results in increased intensities in this location. Remote Palpation will ideally be implemented by holding the transducer in a stationary position, and using electronic focusing to apply radiation force to multiple pushing locations within an extended Field Of View (FOV). The implications of Figure 5 are that some type of depth/focal position dependent scaling may be necessary to achieve a uniform displacement map in a homogeneous medium. This would be similar to Time Gain Control (TGC), which is available on diagnostic scanners to account for tissue attenuation and focal gain. These results also suggest that a two-dimensional array capable of electronically focusing in both the lateral and elevation dimensions is preferable to a linear array.

Evaluation of the steady state displacements shown in the top of Fig. 6 indicates a linear relationship between steady state displacement and acoustic pulse length. Because the same PRF and excitation voltage were used for each pulse, any nonlinearities that were present were the same for all pulse lengths (*i.e.* each pulse had the same peak pressure amplitude). Thus, the ratio of the increase in pulse length, which is approximately equal to the ratio of the increase in intensity, is equal to the increase in radiation force (Eq. 3). Therefore, this

plot portrays a linear relationship between radiation force and intensity, which was predicted by finite element simulations[26].

The bottom plot in Fig. 6 was generated using the same pushing pulses, with different PRFs. Therefore, the intensity was lower for the lower PRFs, which resulted in smaller steady state displacements. Because the PRF of the tracking pulses was fixed at 3584 Hz, which is above Nyquist for each of the pushing pulse PRFs, the bottom plot in Fig. 6 portrays the relaxation of the phantom after each individual pushing pulse. This is apparent in the 'rectified sine wave' that appears on each curve. The low points represent the last track beam fired prior to firing a pushing beam. The PRF of the pushing pulses is identical to the frequency of the 'rectified sine wave' for each curve. It is interesting to note that for each curve, the magnitude of the relaxation increases with increasing mean displacement (*i.e.* the amplitude of the rectified sine wave increases with time). In addition, the magnitude of the 'rectified sine wave' is slightly larger for the lower PRFs. This is due to the relaxation of the tissue between pushing pulses. The longer the time between pushing pulses, the more the tissue relaxes, resulting in a net 'loss' in maximum displacement. This suggests that a more efficient method to implement Remote Palpation will be to use a single, very long pushing pulse, instead of a series of shorter duty cycle pushing pulses (1% to 3% duty cycles) as were used in these experiments.

This point is further demonstrated by evaluating the displacement after the same number of pulses have been fired at two different PRFs (Fig. 6, bottom). For example, at a PRF of 1280 Hz, after 6 milliseconds, 8 pushing pulses have been fired, and the displacement is 45 microns. Correspondingly, 8 pushing pulses have been fired at a PRF of 853 Hz after 8.5 milliseconds, and the displacement is 36 microns. If one computes the temporal average intensity used in both scenarios over 8.5 milliseconds, it is the same. However, by applying the energy initially, instead of evenly spacing it over the entire time, an increase of 20% is achieved in the maximum displacement.

Figure 7 allows the evaluation of the relaxation time of two different phantoms and the liver sample. This quantity is indicative of the damping present in the tissue. The liver

sample is clearly more damped than either of the phantoms, as it has a longer relaxation time. Phantom D exhibits considerably less damping than the other two, in that its relaxation curve appears almost linear.

As stated in the background section, Remote Palpation is similar to elastography, however it has many potential advantages. The fact that the radiation force field is localized and can be applied in selected remote locations is significant. Because the force is applied directly to the position of interest, considerably smaller forces are required than in the case of global compression. Thus one can achieve lesion detectability without exposing the tissue to potentially damaging larger strain fields. In addition, because displacement is directly correlated with local variations in stiffness, the method does not require complex reconstruction algorithms. Finally, in contrast to Elastography, the displacements generated during Remote Palpation are relatively small (microns). Thus the correlation based tracking routines are not subject to problems associated with relative scatterer motion in the presence of large strain[37].

Clinical implementation of Remote Palpation will be similar to conventional mixed modes, such as B-Mode/Color-mode. The physician will identify a smaller FOV within a B-mode image where Remote Palpation will be implemented. Then, upon entering the Remote Palpation mode, the physician will hold the transducer in a stationary position while the FOV is interrogated via electronic focusing and steering. Depending upon the size of the FOV, the spacing of the pushing locations, and the time spent at each location, frame rates as high as 2 to 5 frames per second may be achieved while interrogating a 1.5 cm square FOV. This frame rate will allow the superposition of Remote Palpation displacement images with the conventional B-mode image in semi-real-time, which will aid clinical evaluation.

The resolution achievable by Remote Palpation imaging systems will depend upon a variety of factors, including: the size and spacing of the pushing beams, the resolution and spacing of the tracking beams, the target tissue mechanical properties (Equations 5 and 6), and the methods of image reconstruction utilized. The impact of these factors on resolution is under investigation, however it is outside the scope of this paper.

Given the comparably high intensities and unique pulsing sequences of Remote Palpation imaging, the safety of the method is of concern. The experiments presented herein indicate that Remote Palpation will require *in situ* intensities of up to 300 W/cm^2 at each pushing location. This is well in excess of the FDA limit (0.72 W/cm^2)[29]. However, these high intensity beams need only be generated for time scales on the order of milliseconds. In this short time period, the heating that would be generated is less than 1°C[30], and is limited spatially to a region that is slightly smaller than the focal region of the acoustic beam. Therefore, assuming that adjacent pushing beams do not significantly overlap, the maximum expected temperature rise will be less than 1°C. It is widely accepted that temperature increases of less than 1°C do not pose a danger to the patient[40]. Thus, Remote Palpation imaging as discussed herein should not pose a danger to the patient.

VI. CONCLUSION

The work presented herein clearly demonstrates the feasibility of acoustic Remote Palpation. Displacement maps that are directly correlated with variations in tissue stiffness were generated and presented. It is possible to perform Remote Palpation using a single transducer on a diagnostic scanner to both generate the required high intensity beams, and track the resulting displacements. This will facilitate ease of implementation on transition to the clinical setting. The intensities that are required to induce detectable displacements *in vivo* (*i.e.* tens of microns) will be on the order of 200-300 W/cm^2, and the required dwell time less than 5 milliseconds. Due to the short duration of exposure, these beams should not cause appreciable tissue heating. Given these findings, acoustic Remote Palpation clearly exhibits clinical potential.

VII. ACKNOWLEDGMENTS

This work was supported by DOD BCRP grant BC972755. We thank Siemens Medical Systems, Ultrasound Group for their system support. We thank Intel Corporation for their

technical and in-kind support.

REFERENCES

[1] A. Sarvazyan *et al.*, Acoustical Imaging **21**, 223 (1995).

[2] T. Krouskop *et al.*, Ultrasonic Imaging **20**, 260 (1998).

[3] Y. Yamakoshi, J. Sato, and T. Sato, IEEE Trans. Ultrason., Ferroelec., Freq. Contr. **17**, 45 (1990).

[4] R. Lerner, S. Huang, and K. Parker, Ultrasound Med. Biol. **16**, 231 (1990).

[5] K. Parker, S. Huang, R. Musulin, and R. Lerner, Ultrasound Med. Biol. **16**, 241 (1990).

[6] T. Krouskop, D. Dougherty, and S. Levinson, J. Rehabil. Res. Dev. **24**, 1 (1987).

[7] S. Levinson, J. Biomech. **20**, 251 (1987).

[8] J. Ophir *et al.*, Ultrasonic Imaging **13**, 111 (1991).

[9] M. O'Donnell, A. Skovoroda, B. Shapo, and S. Emelianov, IEEE Trans. Ultrason., Ferroelec., Freq. Contr. **41**, 314 (1994).

[10] J. Ophir *et al.*, Proc. Inst. Mech. Engrs **213**, 203 (1999).

[11] L. Gao, K. Parker, R. Lerner, and S. Levinson, Ultrasound Med. Biol. **22**, 959 (1996).

[12] B. Garra *et al.*, Radiology **202**, 79 (1997).

[13] Westervelt, P.J., J. Acoust. Soc. Am. **23**, 312 (1951).

[14] G. Torr, Am. J. Phys. **52**, 402 (1984).

[15] D. Christensen, *Ultrasonic Bioinstrumentation* (John Wiley & Sons, New York, 1988).

[16] W. Nyborg, in *Physical Acoustics*, edited by W. Mason (Academic Press Inc, New York, 1965), Vol. IIB, Chap. 11, pp. 265–331.

[17] D. Dalecki, Ph.D. thesis, University of Rochester, 1993.

[18] H. Starritt, F. Duck, and V. Humphrey, Phys. Med. Biol. **36**, 1465 (1991).

[19] A. Sarvazyan *et al.*, Ultrasound Med. Biol. **24**, 1419 (1998).

[20] O. Rudenko, A. Sarvazyan, and S. Emelianov, J. Acoust. Soc. Am. **99**, 2791 (1996).

[21] D. Dalecki, E. Carstensen, K. Parker, and D. Bacon, J. Acoust. Soc. Am. **89**, 2435 (1991).

[22] K. Nightingale, P. Kornguth, and G. Trahey, Ultrasound Med. Biol. **25**, 75 (1999).

[23] K. Nightingale and G. Trahey, IEEE Trans. Ultrason., Ferroelec., Freq. Contr. **47**, 201 (2000).

[24] W. Walker, J. Acoust. Soc. Am. **105**, 2508 (1999).

[25] T. Sugimoto, S. Ueha, and K. Itoh, in *Proceedings of the 1990 Ultrasonics Symposium* (PUBLISHER, ADDRESS, 1990), pp. 1377–1380.

[26] K. Nightingale, R. Nightingale, M. Palmeri, and G. Trahey, Ultrasonic Imaging **22**, 35 (January 2000).

[27] M. Fatemi and J. Greenleaf, Proc. Natl. Acad. Sci. **96**, 6603 (1999).

[28] S. Timoshenko and J. Goodier, *Theory of Elasticity* (McGraw-Hill Book Company, New York, 1987).

[29] Center for Devices and Radiological Health (CDRH), U S Dept of Health and Human Services 1985, Rev. 1993, (1994).

[30] M. Palmeri, K. Nightingale, R. Nightingale, and G. Trahey, J. Acoust. Soc. Am. (in preparation).

[31] G. Trahey, J. Allison, and O. VonRamm, IEEE Trans. Biomed. Egr. **BME-34**, 965 (1987).

[32] NEMA Standards Publication/No. UD 2, *Acoustic Output Measurement Standard for Diagnostic Ultrasound Equipment* (National Electrical Manufacturers Association, Washington, D.C., 1992).

[33] F. Duck, UMB **25**, 1009 (1999).

[34] Hall T.J., Bilgen M., Insana M.F., and Krouskop T.A., IEEE Transactions on Ultrasonics, Ferroelectrics and Frequency Control **44**, 1355 (1997).

[35] A. Skovoroda *et al.*, Biophysics **40**, 1359 (1995).

[36] E. J. Chen, J. Novakofski, W. K. Jenkins, and W. D. O'Brien, IEEE Trans. Ultrason., Ferroelec., Freq. Contr. **43**, 191 (1996).

[37] Bilgen M. and Insana M.F., Physics in Medicine and Biology **43**, 1 (1998).

[38] A. Baker, Ultrasound Med. Biol. **23**, 1083 (1997).

[39] W. Walker and G. Trahey, IEEE Trans. Ultrason., Ferroelec., Freq. Contr. **42**, 301 (1995).

[40] NCRP, *Report No. 113: Exposure Criteria for Medical Diagnostic Ultrasound: I. Criteria Based on Thermal Mechanisms* (National Council on Radiation Protection and Measurements, NCRP Publications, Bethesda, MD 20814, 1992).

TABLES

	Gelatin (g)	Water (ml)	N-propanol (ml)	Graphite (g)	Glutaraldehyde (25% soln, ml)	E (kPa)
Tissue (A,B,C)	13.0	230.0	18.0	18.75	52.0	~0.1
Lesion	17.0	222.0	18.0	18.75	60.0	0.5
Tissue (D)	20.0	222.0	18.0	18.75	60.0	1.6

TABLE I.

Table I: Phantom fabrication recipes for 300 milliliters of solution [34].

Figure 1: Percent axial strain (top) and associated axial displacement (bottom) resulting from the application of a point load with a force magnitude similar to that used for Remote Palpation (*i.e.*P=0.01 dynes), in an elastic medium with material properties consistent with those of tissue (*i.e.*ν=0.49, E=30,000 dynes/cm^2 (3.0 kPa))[28]. Note that the axial extent of both fields has decreased to an insignificant amount within 0.2 mm of the location of force application (0mm).

Figure 2: Linear transducer configuration. Note that there is only 1 row of elements, and each element is much taller (elevation dimension) than it is wide (lateral dimension). There is an acoustic lens that focuses in the elevation dimension, and electronic delays are used to focus in the lateral dimension. Thus, the focal point can be varied in the lateral dimension (as was done in Fig. 5), whereas the elevation focal point is fixed.

Figure 3: Schematic of the beam sequences for the different experiments: a) single pushing location with 2-D (B-mode) tracking region, b) single A-line interrogation. The numbers show the spatial relationship between the different lines, and the sequences indicate the temporal order in which the lines were fired. '7p' refers to a pushing pulse that is fired in spatial location 7. The different spatial locations are interrogated by using different sub-apertures (or groups of elements) in the array.

Figure 4: Displacement maps after 10 milliseconds of force application in phantom A. For each of the images, the black contours represent levels of -2 dB and -10 dB of the peak displacement, the lateral focal point was 20 mm, and the transducer was located at the top of the images. a) Displacement profile generated in a homogeneous region of the phantom for an F/1 focal configuration using a single pushing location and a relatively low transmit voltage (29 volts), and a pulse length of 2.2 microseconds. b) Displacement profile generated using the same beam sequence as in a), with the pushing location centered in an 11 mm diameter lesion. The lesion boundaries are highlighted in white. Both a) and b) have the same colorbar scales, ranging from 0 to 3 microns. c) Displacement profile generated in the same location as a), also using an F/1 focal configuration but with a higher transmit voltage (80 volts), and a pulse length of 0.8 microseconds. Note that the displacement profile is similar to a), however it is shorter axially, with the peak shifted slightly closer to the transducer. This is to be expected in the presence of nonlinear propagation. d) Displacement profile generated in the same location as b), using the same beam sequence as in c). Both c) and d) have the same colorbar scales, with displacements ranging from 0 to 18 microns.

Figure 5: Displacement maps generated in calf liver after 10 milliseconds of force application. For each of the images, the black contours represent levels of -1 dB, -3 dB and -6 dB of the peak displacement. The units of displacement on the colorbar are microns. The transducer was located at the top of the images. A constant focal configuration of F/1 was used to generate these images, with a transmit voltage of 140 volts, and a pulse length of 3.3 microseconds. a) lateral focal point at 10 mm. b) lateral focal point at 15 mm. c) lateral focal point at 20 mm. Note that the peak in the displacement map moves with the lateral focal point, and is slightly closer to the transducer than the focal point. This is expected with nonlinear propagation.

Figure 6: Displacement through time near the position of peak displacement (17.5 mm from the transducer) in phantom A. Top: The pulse length of the pushing pulses was varied for each curve as indicated in the legend in units of microseconds, but the PRF was held constant (3584 Hz), as was the focal configuration (F/1) and transmit voltage (140 volts). Note that, as expected, the steady state displacement for the 3.4 microsecond pulse is double that of the 1.7 microsecond pulse. Bottom: For each of these curves, the same pushing pulses were used (F/1 focal configuration, a pulse length of 5.8 microseconds, and a transmit voltage of 140 Volts) but with different pushing pulse PRFs. The frequency of the 'rectified sine wave' apparent in each of the three plots corresponds to the PRF of the high intensity beams for each experiment (as indicated in the legend, in Hz). This is due to the relaxation of the tissue between pushing beams. Note that the magnitude of the relaxation increases over time, with increasing mean tissue displacement.

Figure 7: Displacement over time in the focal region of the transducer for Phantoms A and D in a homogeneous portion of each phantom, as well as in the liver sample. In both Phantom A and the liver sample, the pushing pulses were 3.3 microseconds long, with an F/1 focal configuration and a transmit voltage of 140 volts. In Phantom D, the pushing pulses were 5.8 microseconds long, with an F/1 focal configuration and a transmit voltage of 140 volts. In all experiments the pushing pulses and tracking pulses were interspersed, and the pushing pulses were fired for a total of 52 lines, and then turned off. The PRF in the liver sample was 5120 Hz, whereas in phantoms A and D it was 3584 Hz. The time at which the pushing pulses were turned off has been aligned in these plots for ease of analysis. The dashed lines represent exponential fits to the data. The time constants for the ramp up time are 5.1, 1.6, and 6.2 milliseconds for phantoms A, D, and the liver sample, respectively. The time constants for the relaxation are 4.2, 1.5, and 7.9 milliseconds for phantoms A, D, and the liver sample respectively.

Figure 8: Top left: Grid of pushing locations (9x11 mm, 1mm spacing in both the axial and lateral directions) and their relationship to the lesion. Each dot at the grid intersections represents a pushing location focal point. Although tracking data was obtained throughout the box to either side of each pushing location, only the central tracking line (which is co-located with the pushing line) is shown. Top right: Raw data from fourth row of pushing locations (including all of the lateral tracking lines) used to generate the image shown in Figure 9. Note that although the focal position of the pushing beams is at a fixed range (17mm), the lesion is well defined from 12 to 21 mm axially. Bottom: Each subplot represents the displacement along the axis of the high intensity pushing beam for the 9 axial pushing locations at each lateral position shown on the grid above (a-f). The lesion is clearly apparent as a 'dip' in the displacement profiles in lines a-d, and the width of the 'dip' is consistent with the cross-sectional dimension of the lesion at each lateral location.

Figure 9: a) Displacement image created from multiple pushing locations in phantom C, corresponding to the raw data shown in Fig. 8. The pushing pulses were 1.7 microseconds long, with an F/1 focal configuration and a transmit voltage of 140 Volts. Their PRF was 3584 Hz. The image was created by combining the displacements in each spatial location after 10 milliseconds of force application. The units of displacement on the colorbar are microns. b) Corresponding B-mode image.

Figure 10: a) Displacement image created from multiple pushing locations in phantom B. This phantom had a tear between the lesion and the background material on the left side of the lesion. This resulted in some of the liquid phantom leaking into the tear, and hence a much more compliant region on in the vicinity of the tear. The pushing pulses were 0.83 microseconds long, with an F/1 focal configuration and a transmit voltage of 140 Volts, and a PRF of 3584 Hz. The force applied in this experiment was half of that used to generate the image in Fig. 9. The image was created by combining the displacements in each spatial location after 10 milliseconds of force application. The units of displacement on the colorbar are microns. b) Corresponding B-mode image.

FIGURES

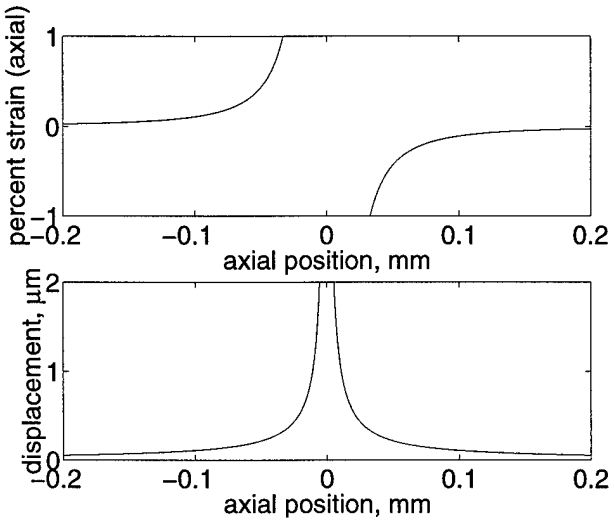

FIG. 1.

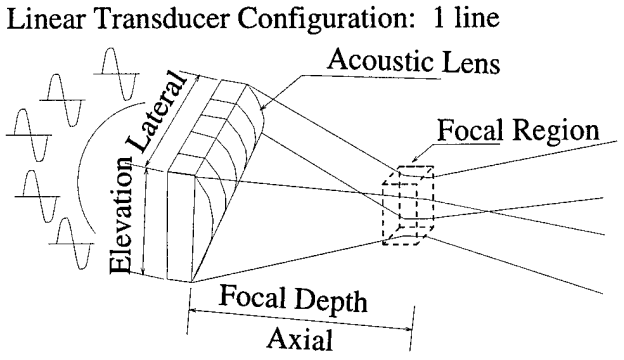
Linear Transducer Configuration: 1 line
Acoustic Lens
Focal Region
Lateral
Elevation
Focal Depth
Axial

FIG. 2.

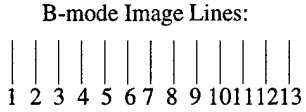

2-D Tracking Region Sequence (13 lines):

1, 2, 3, 4, 5, 6, 7, 8, 9, 10, 11, 12, 13, (track)
7p, 7p, 7p, 7p, ... ,7p, 7p, (7p = push at line 7)
1, 7p, 2, 7p, 3, 7p, 4, 7p, 5, 7p, 6, 7p, (interspersed track/push)
7, 7p, 8, 7p, 9, 7p, 10, 7p, 11, 7p, 12, 7p, 13,
7p, 7p, 7p, 7p, ... (repeat push and interspersed track/push)

Single A-line interrogation (only line 7):

7, 7p, 7, 7p, 7, 7p, ...

FIG. 3.

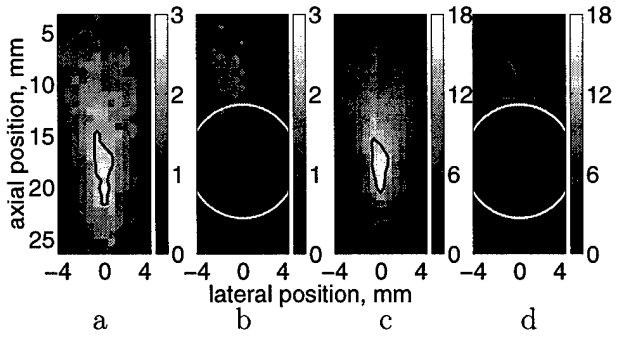
axial position, mm
5
10
15
20
25
−4 0 4
3
2
1
0
18
12
6
lateral position, mm
a
b
c
d

FIG. 4.

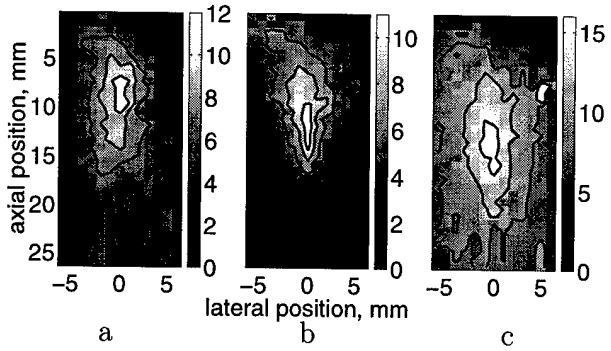
axial position, mm
5
10
15
20
25
−5 0 5
12
10
8
6
4
2
0
lateral position, mm
a
b
c
15
5

FIG. 5.

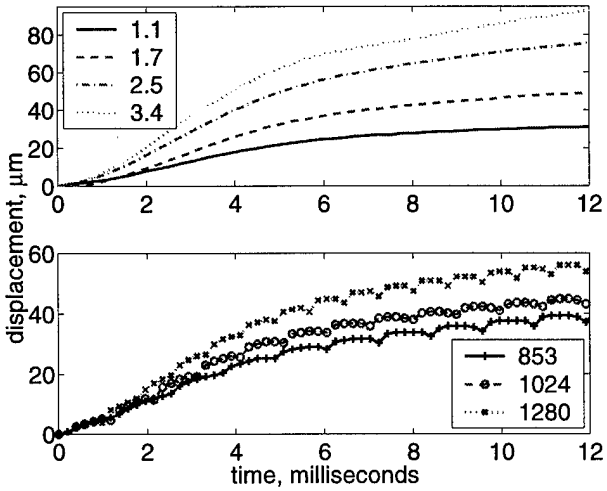
1.1
1.7
2.5
3.4
853
1024
1280
displacement, µm
time, milliseconds
0
20
40
60
80
0
2
4
6
8
10
12

FIG. 6.

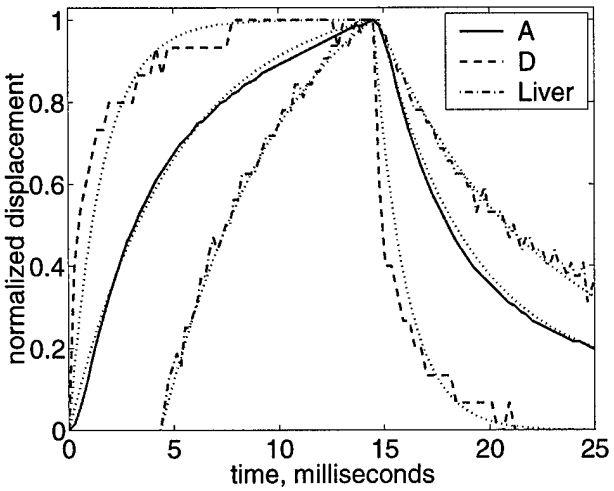
A
D
Liver
normalized displacement
time, milliseconds
0
0.2
0.4
0.6
0.8
1
0
5
10
15
20
25

FIG. 7.

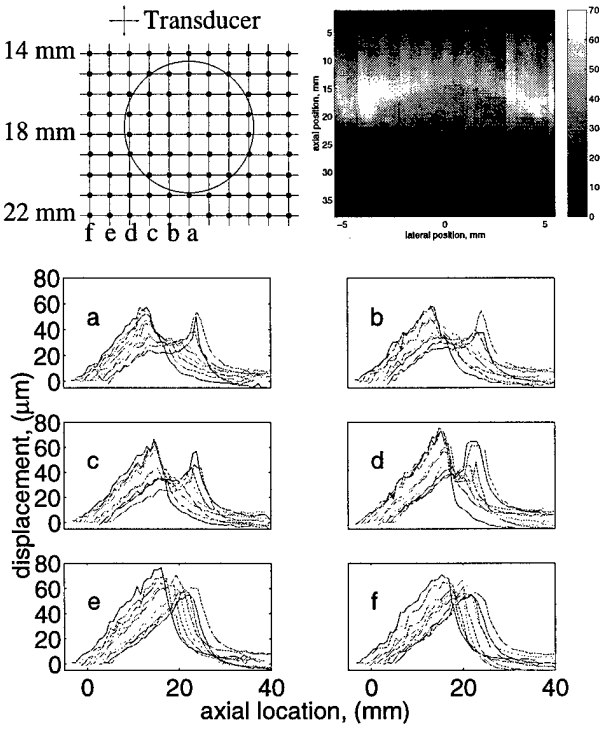
Transducer
14 mm
18 mm
22 mm
f e d c b a
axial position, mm
lateral position, mm
displacement, (μm)
axial location, (mm)
a
b
c
d
e
f

FIG. 8.

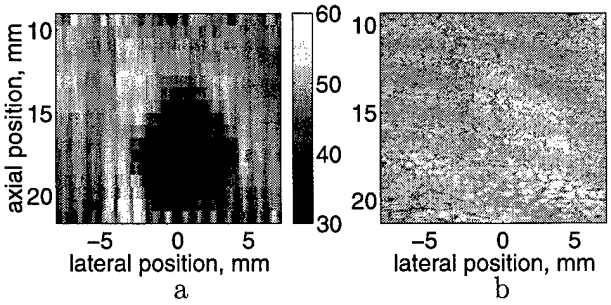
axial position, mm
10
15
20
60
50
40
30
−5
0
5
lateral position, mm
a
10
15
20
−5
0
5
lateral position, mm
b

FIG. 9.

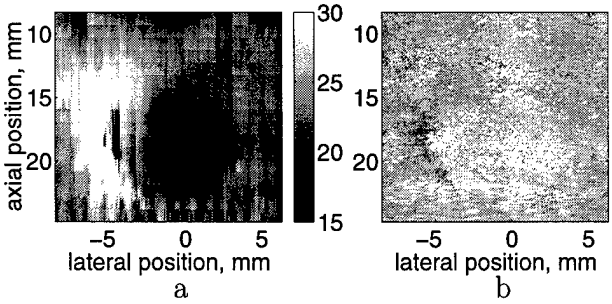
axial position, mm
10
15
20
30
25
20
15
−5
0
5
lateral position, mm
a
10
15
20
−5
0
5
lateral position, mm
b

FIG. 10.